AD_____

AWARD NUMBER: W81XWH-08-1-0613

TITLE: X-Ray Phase Imaging For Breast Cancer Detection

PRINCIPAL INVESTIGATOR: Xizeng Wu, Ph.D.

CONTRACTING ORGANIZATION: University of Alabama at Birmingham
                                                      Birmingham, AL 35294

REPORT DATE: September 2009

TYPE OF REPORT: Annual

PREPARED FOR: U.S. Army Medical Research and Materiel Command
                         Fort Detrick, Maryland 21702-5012

DISTRIBUTION STATEMENT: Approved for Public Release;
                                         Distribution Unlimited

REPORT DOCUMENTATION PAGE

1. REPORT DATE	2. REPORT TYPE	3. DATES COVERED
1 September 2009	Annual	1 Sep 2008 – 31 Aug 2009

4. TITLE AND SUBTITLE	5a. CONTRACT NUMBER
X-Ray Phase Imaging For Breast Cancer Detection	5b. GRANT NUMBER W81XWH-08-1-0613
	5c. PROGRAM ELEMENT NUMBER
6. AUTHOR(S)	5d. PROJECT NUMBER
Xizeng Wu, Ph.D.	5e. TASK NUMBER
E-Mail: xwu@uabmc.edu	5f. WORK UNIT NUMBER

7. PERFORMING ORGANIZATION NAME(S) AND ADDRESS(ES)	8. PERFORMING ORGANIZATION REPORT NUMBER
University of Alabama at Birmingham Birmingham, AL 35294	

9. SPONSORING / MONITORING AGENCY NAME(S) AND ADDRESS(ES)	10. SPONSOR/MONITOR'S ACRONYM(S)
U.S. Army Medical Research and Materiel Command Fort Detrick, Maryland 21702-5012	
	11. SPONSOR/MONITOR'S REPORT NUMBER(S)

12. DISTRIBUTION / AVAILABILITY STATEMENT
Approved for Public Release; Distribution Unlimited

13. SUPPLEMENTARY NOTES

14. ABSTRACT
The long term objective of the project is to develop a low-dose and quantitative phase x-ray imaging technique for facilitating breast cancer detection. Phase retrieval from a single phase contrast image is the key strategy for this project. In this period we have accomplished following tasks: (1). Successfully developed a new phase retrieval method with a full account of the nonlinear Fresnel propagators. This new phase retrieval method provides the scientific foundation and framework for developing new and more accurate phase retrieval algorithms for this project. (2). Conducted the system design study for the project. Importantly we have determined the optimal imaging geometry based on the quantitative phase contrast visibility analysis. (3). Conducted system hardware integration. A prototype is developed and the tests showed that the prototype is well functioning for phase contrast image acquisition. In the coming year we will conduct phase imaging experiments with custom-made breast phantoms. Especially we will incorporate the measured source incoherence effects and CR-detector response effects into the phase retrieval algorithms for accurately reconstruction of the maps of projected electron densities of the phantoms.

15. SUBJECT TERMS
Phase-contrast x-ray imaging, Breast imaging, Phase retrieval

16. SECURITY CLASSIFICATION OF:			17. LIMITATION OF ABSTRACT	18. NUMBER OF PAGES	19a. NAME OF RESPONSIBLE PERSON USAMRMC
a. REPORT	b. ABSTRACT	c. THIS PAGE	UU	26	19b. TELEPHONE NUMBER *(include area code)*
U	U	U			

Table of Contents

Introduction

Currently breast cancer screening is performed using x-ray mammography, including both the screen-film based mammography and digital mammography. These two x-ray mammography modalities all rely on small differences in the linear attenuation coefficients between adipose and glandular tissues to produce the mammogram. Breast is one of the most difficult human organs for x-ray imaging, since it consists of tissues with similar densities and attenuation coefficients, resulting in low contrast. However, as x-ray wave passes through tissues, x-ray undergoes phase-shifts as well. The amount of the phase shift is determined by tissue's refractive index and the ray path length. The refractive index n for x-ray is complex : $n = 1 - \delta + i\beta$, where δ is the refractive index decrement determined by x-ray wavelength and tissue electron density, is responsible for x-ray phase shift, and β is the imaginary part of the refractive index and it is responsible for x-ray attenuation. The amount of x-ray phase shift from a piece of tissue is given by $\phi = -\left(2\pi/\lambda\right)\int \delta(s)ds = -\lambda r_e \int \rho_e(s)ds$, where λ denotes x-ray wavelength, r_e the classical radius of electron, ρ_e tissue's electron density, and the integral is taken over the ray path. Consider the infiltrating ductal carcinoma (IDC) in breast, we found that its δ is about 1000 times greater than its β for x-rays of 10 keV-150 keV [30]. Similar conclusions can be drawn for other biological tissues. It is ironical that the current mammography techniques are designed to image a tissue's β but not its δ . Hence the phase sensitive x-ray imaging has potential for greatly increasing x-ray imaging sensitivity and specificity and reducing radiation doses associated with the imaging.

The approaches for phase-sensitive x-ray imaging currently under investigation fall into three broad categories: interferometric imaging, diffraction-enhanced imaging, and inline phase-sensitive imaging. The technique being developed in this project falls into the category of inline phase-sensitive imaging, which is in general based on the inline holography principle in optics. In inline imaging the diffracted x-ray with shifted phases forms bright and dark fringes at tissue boundaries. The edge enhancement thus generated relies on the spatial coherence of the x-ray source, the optimal positioning of detector, and the x-ray energy. The inline phase-sensitive imaging requires neither expensive crystal analyzers nor the fabrication-challenging gratings as other techniques do. For the inline phase-sensitive imaging, the spatial coherence of x-rays is more important than its temporal coherence. Furthermore, the spatial coherence offered by a synchrotron radiation source can also be obtained with a x-ray tube with a small focal spot size and relatively large source-to-detector distance. Of course this approach for achieving x-ray spatial coherence is constrained by the requirement of sufficient photon-flux required for achieving short exposure time for clinical imaging.

The long term objective of the project is to develop a low-dose and quantitative phase x-ray imaging technique for facilitating breast cancer detection. The Specific Aims of the project of the three-year period are: (1) Develop prototype phase-imaging system enabling the phase retrieval, that is, the reconstruction of objects phase-maps. The system hardware comprises a micro-focus tube operating at high tube voltages, a high resolution photostimulable phosphor plate (CR-plate) based detector system. The core algorithms for breast phase-map reconstruction will be developed to retrieve a breast phase map from a single recorded image. (2) Validate the accuracy of the reconstructed tissue projected electron densities; validate the many-fold radiation dose reduction achieved with the proposed system; conduct subjective measurements to characterize the performance of the proposed system.

Body

In the first year of this project, as planned in the Statement of Work, we performed two tasks: (A). Develop the phase retrieval algorithms for future phase imaging with breast phantoms; (B). Design and build the system hardware for future phase imaging with breast phantoms.

(A). Develop the phase retrieval algorithms

Phase contrast x-ray imaging requires a x-ray source proving highly spatially coherent illumination of the imaged object. With a micro-focus x-ray tube the achievable x-ray spatial coherence is very limited, hence the phase-contrast imaging with a x-ray tube source can generate only a limited phase-contrast mixed with the attenuation contrast. The contrast enhancement at tissue interfaces and boundaries generated by the dark-bright diffraction fringes are still limited. On the other hand, the phase imaging technique that we proposed goes behind the phase-contrast imaging. By means of phase retrieval from acquired phase-contrast images, one can disentangle the high phase contrast from the mixed contrast mechanisms presented in the phase-contrast image. Moreover, a retrieved tissue phase map provides a map of imaged object's projected electron densities (the ray integrals of electron densities) as well.

The ch allenge for dev eloping br east x -ray phase i maging is how t o overcome the difficulty f or i mplementing phase r etrieval with breast i maging.   In or der t o co mpletely disentangle tissue phase-shifts from the mixed contrast in acquired phase-contrast images, in general one needs to acquire at least two and m ostly four to five images with different object-detector distances.   This requirement is imposed by the x-ray wave nature and its wave equation. This cumbersome procedure delivers higher radiation dose to breast and makes the images su sceptible t o t he m otion a rtifacts.   Therefore, an i mportant c hallenge i s to find a n effective and low-dose approach for phase retrievals.

Phase retrieval from a single phase contrast image is the key strategy for this project. We previously studied how high energy x-ray wave propagates in tissues. Analyzing the tissue attenuation data, we realized that the soft tissue attenuation cross sections are approximate by that fr om x-ray i ncoherent s cattering f or x-rays of abou t 60   keV or higher.   Under t his circumstance**,** we found that soft-tissue attenuation and so ft-tissue phase ar e all related to the projected electron density, we call this new notion as the phase-attenuation duality**.** Based on this notion of the phase-attenuation duality, we discovered a new innovative way to retrieve a phase-map f rom j ust a si ngle recorded image [Wu et al. 2005].   In t his way t he pr oblems associated with the requirement of multiple-image acquisition for phase-retrieval is eliminated. Recently we noted that our previous phase retrieval method, though performed phase-retrieval very well i n g eneral from onl y a si ngle phase -contrast i mage, i s not ac curate enou gh for t he cases with h igh sp atial r esolution and large o bject-detector di stances. I n or der t o dev elop robust algorithms with high accuracies in breast phase map retrieval, in this period of the project we investigated and developed a new and more accurate phase retrieval method based on the phase-attenuation duality.

Method: The physics behind our method developed in this project can be explained as follows. The phase contrast is formed by the phase-shifted x-ray's Fresnel diffraction from the

object to the detector. The enhanced tissue phase contrast is manifested as the formation of bright and dark diffraction fringes in the measured images. Our task is to determine the map of tissue phase-shifts from these enhanced image intensity variation. We noticed that in the transverse spatial-frequency space (the transverse k-space) the Fresnel diffraction can be thought as a x-ray wave-front filtering with the Fresnel propagator $\exp(i\pi\lambda z\vec{u}^2)$, where λ is x-ray wavelength and $\vec{u}$ is the wave-front's transverse spatial frequency vector, and z is the object-detector-distance. So the phase of the propagator, i.e. $\pi\lambda z\vec{u}^2$, determines how strongly the exiting wave-front will be diffracted in the propagation. Our previous phase retrieval formula was derived by linearizing Fresnel propagator phases for simplifying the x-ray wave equation, or the transport-of-intensity equation [Wu et al. 2005]. Therefore, in order to develop robust algorithms with high accuracies for breast phase map retrieval, one cannot linearize Fresnel propagators, rather one should consider the full exponential propagators instead, with a price of dealing a much more complicated x-ray wave equation. We then used the phase-attenuation duality to delineate the complicated equation for deriving a new phase retrieval formula.

Result: Our research efforts through the first period of this project eventually paid off: we successfully developed a new phase retrieval method with a full account of the nonlinear Fresnel propagators. This new phase retrieval method provides the scientific foundation and framework for developing new and more accurate phase retrieval algorithms for this project. The computer simulation demonstrated superiority of this new method over our previous duality-based phase-retrieval formula in reconstructing the high frequency components of imaged objects. In addition, this new phase retrieval method lays the foundation for implementing high-resolution phase-sensitive volumetric imaging (CT and tomosynthesis) of soft tissue objects as well. Our work was published in *Optics Express* in June 2009 [Wu et al. 2009]. The paper is enclosed in the Appendix of this report for review.

Emanating from this result, as a by-product of this project, we have applied our phase retrieval method to the phase sensitive tomography as well. Previously several group reported that in the phase-contrast CT experiments images reconstructed with the standard filtered backprojection algorithms suffered from erroneous artifacts such as the streaks and negative densities. We believed that these artifacts arise from the fact that x-ray does not propagate along straight lines in phase-contrast projections, because x-ray refracts and diffracts at tissue interface and boundaries. In order to correctly deal with the issue of phase-contrast tomography reconstruction, one should first retrieve the phase maps for all projections, then reconstruct the image-slices of tissue attenuation coefficients and electron densities, respectively. However, multiple image-acquisitions required for phase retrievals make the implementation very cumbersome, since multiple phase-contrast images have to be acquired for each projection view during a source sweep. Moreover, radiation dose to breast will be multiplied for the multiple image acquisition per projection view. Therefore, the phase retrieval method reported here for this project can greatly facilitate the artifact-free phase-sensitive CT. By computer simulation we showed how the artifacts get generated in phase-contrast CT and how our phase retrieval method developed for this project provided artifacts-free accurate CT image reconstructions. We reported this progress at the 2009 AAPM annual meeting in July 2009. The peer-reviewed abstract of this oral presentation was published in *Medical Physics* and is enclosed in the Appendix as well.

(B). Design and build the system prototype

The system design study and system hardware integration have been conducted in this period.

(1). Study on the system design

Determine Imaging Geometry : Different from conventional x-ray imaging, the phase contrast imaging needs adequate spatial coherence of x-rays illuminating the breast, hence it
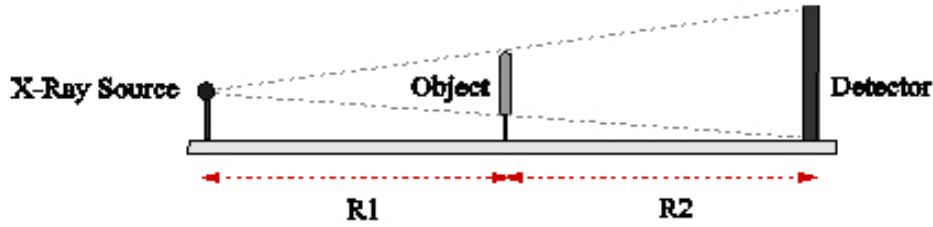
Figure 1. Geometry Setting of the phase imaging prototype.   The source-object distance is denoted by R_1**, and the object-detector distance by** R_2.

requires a micro-focus tube as the source , and a large source-object distance **R_1** as is shown in the Fig. 1.   The object to detector distance **R_2** should be sufficiently large as well to allow phase-shifted x-rays to diffract as forming a phase-contrast image. Considering future clinical application, we use a source to image-receptor distance (SID) of 1.5 m - 1.8 m. Selecting optimal values of the distances **R_1** and **R_2** is crucial for successful phase contrast imaging. This is because the imaging-geometry should optimize the phase contrast visibility by balancing the conflict requirements of x-ray spatial coherence, large diffraction fringes and finite sizes of the focal spot size and finite detector pitch. In a previous work we found that the phase-contrast that could be imaged is proportional to the relative phase-visibility factor (RPF) and its modulus is $\left| RPF(\vec{u}) \right| = c^2 h^2 MTF_{G.U.}\left(\vec{u}/M \right) MTF_{\det}\left(\vec{u}/M \right) \left[\int \left(\pi R_2 \vec{u}^2 / ME^2 \right) S(E) dE \right]$, [Wu et al. 2004].

In this formula h is the Planck constant and c the speed of light, $\vec{u}$ the spatial frequency vector of a fine object structure to be imaged, M is the magnification factor, E x-ray photon energy, and S(E) is the x-ray spectrum. In addition, $MTF_{G.U.}(\vec{u})$ denotes the MTF of the geometric unsharpness due to the focal spot size, and $MTF_{\det}(\vec{u})$ is the MTF of the detector. For a given object structure to be imaged, the larger $\left| RPF(\vec{u}) \right|$ a system-configuration achieves, the more the phase-contrast manifests with this configuration, though the actual phase-contrast exhibited in an image depends on the imaged object's phase variation as well. The higher $\left| RPF(\vec{u}) \right|$ is the more the phase-contras manifests. Therefore the relative phase-visibility factor $\left| RPF(\vec{u}) \right|$ provides a very useful tool for designing a phase-contrast imaging system.   We studied the $\left| RPF(\vec{u}) \right|$ for this project and a typical data from the study is plotted as shown in Fig. 2 below, where we assumed a source-detector distance SID = 1.5 m, a uniform circular focal spot of 50 μm in diameter, and a detector pitch of 43.75 μm. These parameters are according to the specs of the available micro-focus tube and imaging detector.   In addition, we assumed 60.5 keV x-ray and a fine object structure of 15 line-pairs/mm. We found that the MTF of the geometric unsharpness is $MTF_{G.U.}(\vec{u}) = \left[2J_1(\pi f (M-1)|\vec{u}| / M) \right] / \left[\pi f (M-1)|\vec{u}| / M \right]$, where f is the diameter of the focus spot, and $J_1(x)$ is a Bessel function of the first kind. We used the

sin*c*-function for modeling the $MTF_{\text{det}}(\vec{u})$. Fig. 2 shows the computed $\left|RPF(\vec{u})\right|$ plot for a fine structure of 15 line-pairs/mm. We found that the $\left|RPF(\vec{u})\right|$ peaks for **R$_1$** = 0.65 m, and **R$_2$** = 0.85 m, that is, with the magnification factor M = 2.31 for 60.5 keV x-ray. This maximal phase visibility is a 83% increase compared to the phase visibility with **R$_1$** = 1.1 m and **R$_2$** = 0.4 m (M = 1.36.) The results show as well that the phase visibility will decrease if the magnification factor exceeds 2.35. Therefore, our reference design adopts system geometry parameters ranging from **R$_1$** = 0.7 m, and **R$_2$** = 0.8 m to **R$_1$** = 0.65 m, and **R$_2$** = 0.85 m.
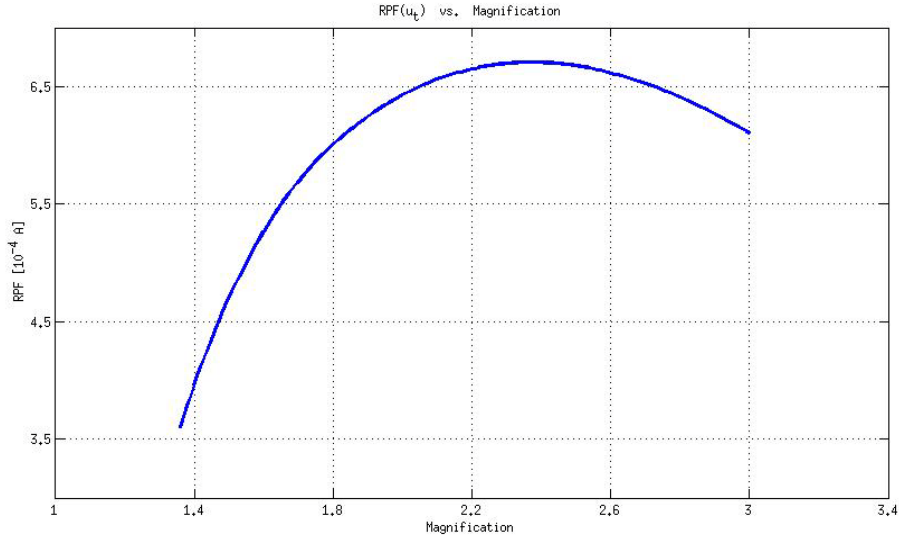
Figure 2. Relative phase contrast visibility $\left|RPF(\vec{u})\right|$ varies for different imaging geometry parameters (**R$_1$** and **R$_2$**) of the prototype system. In this plot we assumed a source-detector distance of 1.5 m, a uniform circular focal spot of 50 μm in diameter, and a detector pitch of 43.75 μm , 60.5 keV x-ray and a fine object structure of 15 line-pairs/mm.

According to above analysis and the hardware availability in the lab, the system hardware components to be employed for this project are described as follows.

X-Ray Tube**:** We employ a micro-focus tube (Model L8121-01, Hamamatsu Photonics) with integrated high voltage power supply. The tube has a tungsten-target and a uniform circular focal spot of 50 μm in diameter. The tube can operate at 150 kVp with maximal tube current 0.5 mA. The target angle is 25$^{\text{o}}$. Our test showed that with such a tube operating at 120-150 kVp breast phantom images can be acquired with a exposure of few seconds.

Image Detector**:** Since tissue phase-contrast fringes recorded is proportional to the Laplacian and gradient of phase-shifts, hence the detector should have high sampling frequency. We employ a Konica Minolta Konica 24 x 30cm photostimulable phosphor plate (CR-plate) and a Konica REGIUS 190 Reader of a 43.75 μm sampling pitch.

Image Display System**:** For the high resolution mage-display of the full size images we will use the GE Seno Advantage review workstation (RWS) in the Radiology department of

University of Alabama at Birmingham. The RWS has two monitors and each is a grayscale high-resolution 5 M pixels (2560 x2048) CRT-monitor.

(2). Integrating the system components to a prototype system

Since the project does not support equipment purchase, most of the system components are those available from our subcontractor Dr. Liu's laboratory at University of Oklahoma. Dr. Liu group performed the works of integrating the hardware components to a prototype system.

Mounting the System on An Optical Bench: In order to operate the prototype in both conventional and phase contrast imaging modes for comparisons, the imaging and measurement components (the x-ray tube, CR-plate) are mounted on an optical rail, which allows to vary a large source-object distance R_1 and object-detector distance R_2 as needed. It is also to allow use of a precise laser alignment process for later measurements of x-ray spectra and system's detective quantum efficiency (DQE).

The source is a micro-focus tube (Model L8121-01, Hamamatsu Photonics) with integrated high voltage power supply. The tube has a tungsten-target and a uniform circular focal spot of $50\,\mu m$ in diameter. The tube can operate at 150 kVp with maximal tube current 0.5 mA. During the hardware integration, the tube assembly malfunction occurred, and eventually the tube assembly and its controller failed. After tedious efforts in dealing with the OU offices and the vendor (Hamamatsu Photonics) for the repair costs and repair arrangements, the source assembly is currently in Hamamatsu's shop for repair and calibrations. As a replacement tube for the time being, the prototype utilizes an micro-focus tube with a Molybdenum anode and a Beryllium output window (UltraBright Microfocus Source, Oxford Instruments, Scotts Valley, California). The x-ray tube can be operated between 20 and 60 kVp and between 10 and 60 W. For the tests performed the 20 W-mode was utilized, and in this mode the diameter of the focal spot is $20\,\mu m$. Due to the limitations of the source, the high energy x-ray in testing was that from the tube operating at 60 kVp only. The tube voltage, tube power, and exposure time are controlled precisely by a software application interfacing directly with the source.

The mounted detector is a Konica Minolta Konica 24 x 30cm photostimulable phosphor plate (CR-plate) and a Konica REGIUS 190 Reader of a $43.75\,\mu m$ sampling pitch.

Prototype Testing: In order to demonstrate the functionality of the integrated hardware component, phantom phase contrast imaging experiment were performed.

(a). A Tissue-Equivalent Breast Phantom: The Mammography BR3D phantom (Model 020, CIRS, Norfolk, Virginia) was utilized for the experiment. The BR3D phantom, as a tissue-equivalent phantom, was fabricated from materials simulating 100% adipose and glandular tissues blended together in an approximate 50/50 ratio by weight, which produces a tissue-equivalent heterogeneous background on an x-ray image. The phantom consists of a set of five pieces of the same size, each having a thickness of 10 mm and a different blend of the materials. The combination of the five layers was designed to produce realistic tissue-equivalent x-ray images. The qualitative comparison was performed for a high energy phase contrast image and a low energy conventional radiograph. The ability to distinguish structures within the images will provide a visual indication of the relative image quality. The conventional radiograph of the tissue-equivalent phantom acquired by low energy (20 kVp) conventional

contact mode ($M = 1$), is shown in Fig. 3-(left). The phase contrast image of the phantom acquired with high energy (60 kVp) and $R_1 = R_2 = 91.4$ cm is shown in Fig. 3-(right). The qualitative comparison illustrates improved tissue-material contrast in the phase contrast image as compared to the conventional radiograph, although the conventional radiograph was acquired at much lower tube voltage (20kVp) and it would have more attenuation-contrast compared to an image acquired at 60 kVp. The testing shows the prototype functioning well.
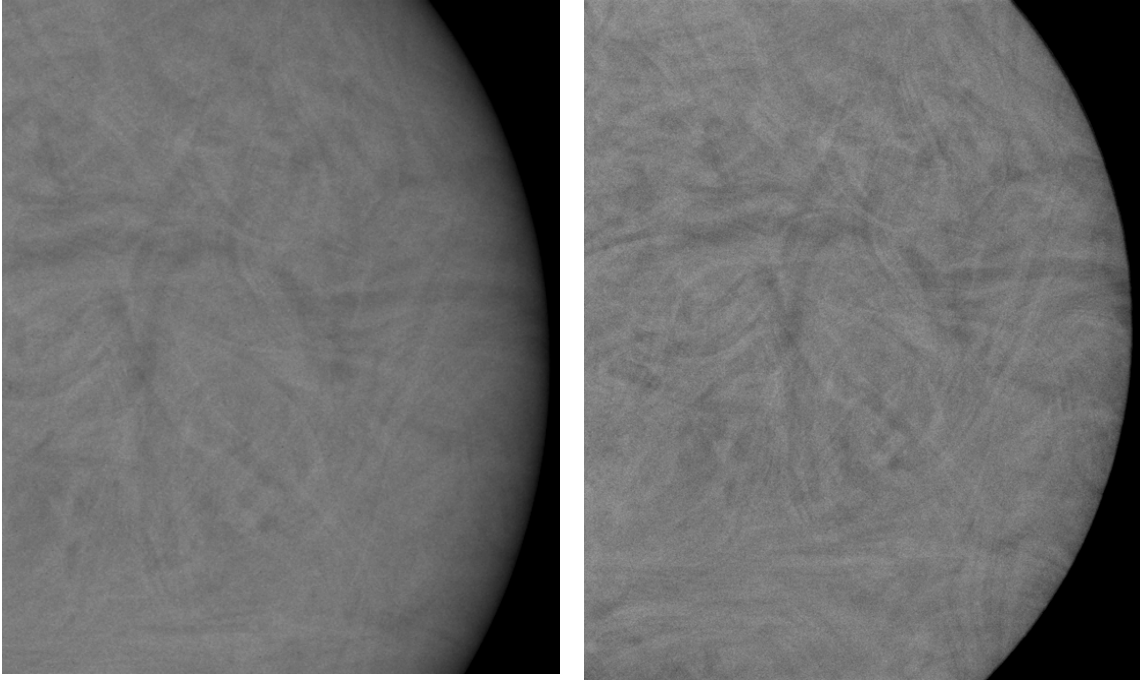

Figure 3. Acquired Images of a Mammography BR3D phantom. (left): the image acquired at 20 kVp, 20 W in conventional contact mode; (right): the image acquired at 60 kVp, 20 W with $R_1 = R_2 = 91.4$ cm in the phase contrast mode.

(b). An Acrylic Edge Phantom: A laser-cut sharp edge of a thin acrylic plate (~1.5 mm) provides a phase step: a phase jump from acrylic plate to air along the sharp edge. The conventional radiograph of the edge phantom acquired by low energy (20 kVp) conventional contact mode ($M = 1$), is shown in Fig. 4-(left). The phase contrast image of the phantom acquired with high energy (60 kVp) and in phase contrast mode is shown in Fig. 4-(right). Compared to the conventional radiograph of the acrylic edge shown in Fig. 4-(left), the phase contrast image of the same phantom at 60 kVp (Fig. 4-(right)) shows less large-area attenuation contrast as is expected. However, the phase contrast image in Fig. 4-(right) uniquely demonstrates the signature bright-dark fringes flanking the phase step edge. The diffraction fringes is proportional to the Laplacian of the phase step. In fact, the intensity profile along a orthogonal line across the edge in Fig. 4-(right) demonstrates a downward overshooting and followed by an upward overshooting in the phase contrast image (Fig. 5-(right).). But such overshooting disappears in the intensity profiles of conventional radiograph (Fig. 5-(left).)
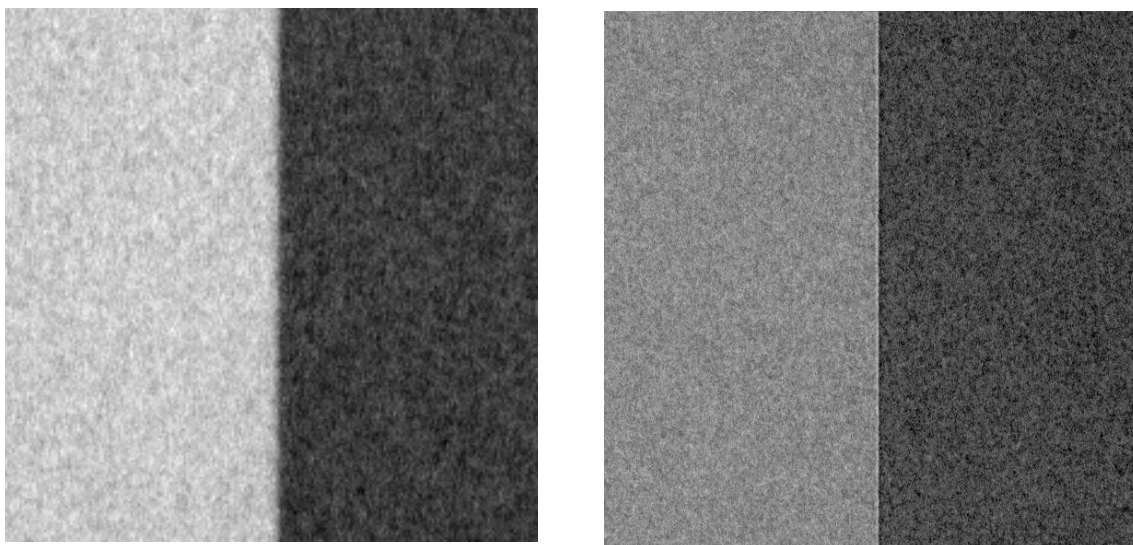
Figure 4. Acquired Images of a phase-step edge phantom.   (left): the image acquired at 20 kVp, 20 W in conventional contact mode; (right): the image acquired at 60 kVp, 20 W in phase contrast mode ($R_1 = R_2$ = 91.4 cm.)
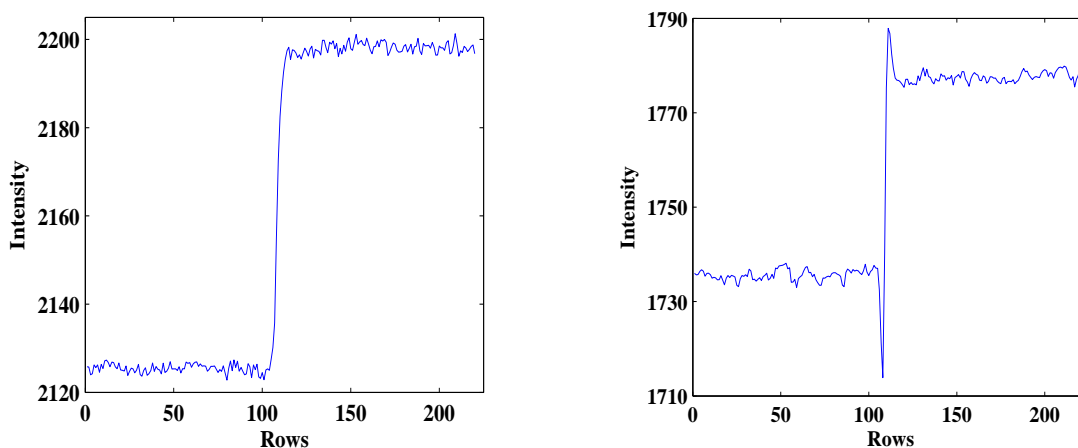

Figure 5. (left): the intensity profile across the edge for the conventional radiography in Fig. 4-(left); (right): the intensity profile across the edge for the phase contrast image in Fig. 4-(right).

In summary, the system hardware integration has been conducted in this period. A prototype is developed and the tests showed that the prototype is functional for phase contrast image acquisition.   Once the in-repair micro-focus tube (Model L8121-01, Hamamatsu Photonics) is returned back from Hamamatsu company, we will soon be ready to acquire phase contrast images at 120-150 kVp as designed.   In addition, we will continue to experiment the

ways to match the CR-plate's quantum detection efficiencies with the designed high energy x-rays and keep reading the CR-plates in the high sampling mode of the Konica REGIUS 190 Reader.

Key Research Accomplishments

- Phase retrieval from a single phase contrast image is the key strategy for this project. In this period we successfully developed a new phase retrieval method with a full account of the nonlinear Fresnel propagators.   This new phase retrieval method provides the scientific foundation and framework for developing new and more accurate phase retrieval algorithms for this project. The computer simulation demonstrated superiority of this new method over our previous phase-retrieval method in reconstructing the high frequency components of imaged objects.

- Conducted the system design study for the project.   Especially we have determined the optimal imaging geometry based on the quantitative phase contrast visibility analysis.

- Conducted system hardware integration. A prototype is developed and the tests showed that the prototype is well functioning for phase contrast image acquisition.

Reportable Outcomes

In this project period we have published the research results in peer-reviewed journals and presented the work in an international conferences, as listed in the following.

Peer-Reviewed Journal Article**:**

X. Wu and A. Yan: "Phase retrieval from one single phase contrast x-ray image," *Optics Express* 17: 11187-11196 (2009).

This journal is the top-ranking journal in terms of the Impact Factor among all sixty-four journals in the field of Optics.

Published Abstract and Conference Presentation**:**

X. Wu, A. Yan , H. Liu: "Contrast mechanism and origin of artifacts in phase-sensitive x-ray volumetric imaging", *Medical Physics* 36: 2785 (2009).

X. Wu, A. Yan , H. Liu: "Contrast mechanism and origin of artifacts in phase-sensitive x-ray volumetric imaging." Oral Presentation at the 51st Annual Meeting of the American Association of Physicists in Medicine, July 29, 2009, Anaheim, California

Conclusion

With the support by USAMRMC we have successfully conducted studies on x-ray phase imaging in the first period of this project. As the key strategy of the project is to perform the phase retrieval from a single phase contrast image, in this period we successfully developed a new phase retrieval method from a single image with a full account of the nonlinear Fresnel propagators. This new phase retrieval method provides the scientific foundation and framework for developing new and more accurate phase retrieval algorithms for this project. The computer simulation demonstrated superiority of this new method over our previous phase-retrieval method in reconstructing the high frequency components of imaged objects.

In this period we have conducted the system design study. The crucial focus of the system design is to determine the imaging-geometry, which should optimize the phase contrast visibility by balancing the conflict requirements of x-ray spatial coherence, large diffraction fringes while being constrained by the finite sizes of the tube focal spot and detector-pitch. We investigated how the relative phase-visibility factor varies with system hardware parameters and found the optimal reference imaging geometry parameters for the project. To implement the system design, a prototype has been built by integrating the system components. With the system prototype phase contrast images were acquired with different phantoms for verifying the prototype's functionality.

In the coming year we will continue the efforts in improving the prototype's performance, especially work with the repaired tube operating on the designed high tube voltages, and with the matched CR plates readable with the high sampling mode. We will conduct phase imaging experiments with custom-made breast phantoms, and will reconstruct the phase maps of the phantoms. Especially we will incorporate the measured source incoherence effects and the detector response effects into the phase retrieval algorithms for accurate phase retrieval. We will start to experimentally verify the accuracies of the reconstructed maps of the projected electron densities of the imaged phantoms.

References

Wu, X., Liu, H. 2004. A new theory of phase-contrast x-ray imaging based on Wigner distributions. *Medical Physics* 31, 2378-2384.

Wu, X., Liu, H., Yan, A. 2005. X-Ray phase-attenuation duality and phase retrieval. *Optics Letters* 30, 379-381.

Wu, X., Yan, A. 2009. Phase retrieval from one single phase contrast x-ray image, *Optics Express* 17, 11187-11196.

Appendices

Copies of following publications are enclosed for review.

<u>Peer-Reviewed Journal Article</u>**:**

X. Wu and A. Yan: "Phase retrieval from one single phase contrast x-ray image," *Optics Express* 17: 11187-11196 (2009)

<u>Published Abstract</u>**:**

X. Wu, A. Yan, H. Liu: "Contrast mechanism and origin of artifacts in phase-sensitive x-ray volumetric imaging", *Medical Physics* 36: 2785 (2009).

Phase retrieval from one single phase contrast x-ray image

Xizeng Wu and Aimin Yan

Department of Radiology, University of Alabama at Birmingham, Birmingham, AL 35233, USA

xwu@uabmc.edu, ayan@uabmc.edu

Abstract: Phase retrieval is required for achieving artifact-free x-ray phase-sensitive 3D imaging. A phase-retrieval approach based on the phase-attenuation duality with high energy x-rays can greatly facilitate for phase sensitive imaging by allowing phase retrieval from only one single projection image. The previously derived phase retrieval formula is valid only for small Fresnel propagator phases corresponding to common clinical imaging tasks. In this work we presented a new duality-based phase retrieval formula that can be applied for cases with large Fresnel propagator phases corresponding to high spatial resolution imaging. The computer simulation demonstrated superiority of this new formula over the previous phase retrieval formula in reconstructing the high frequency components of imaged objects. A modified Tikhonov regularization technique has been devised for phase retrieval in cases of very high resolution and large object-detector distance such that some Fresnel propagator phases may be close or greater than π. This new phase retrieval formula lays the foundation for implementing high-resolution phase-sensitive 3D imaging of soft tissue objects.

© 2009 Optical Society of America

OCIS codes: 340.7440 (X-ray imaging); 030.1670 (Coherent optical effects)

References and links

1. S. Wilkins, T. Gureyev, D. Gao, A. Pogany, and A. Stevenson, "Phase-contrast imaging using polychromatic hard X-rays," Nature **384**, 335 – 338 (1996).
2. A. Snigirev, I. Snigireva, V. Kohn, S. Kuznetsov, and I. Shelokov, "On the possibilities of x-ray phase contrast microimaging by coherent high-energy synchrotron radiation," Rev. Sci. Instrum. **66**, 5486 – 5492 (1995).
3. K. Nugent, T. Gureyev, D. Cookson, D. Paganin, and Z. Barnea, "Quantitative Phase Imaging Using Hard X Rays," Phy. Rev. Lett. **77**, 2961 – 2965 (1996).
4. A. Pogany, D. Gao, and S. Wilkins, "Contrast and resolution in imaging with a microfocus x-ray source," Rev. Sci. Instrum. **68**, 2774 – 2782 (1997).
5. F. Arfelli, V. Bonvicini, and et al, "Mammography with synchrotron radiation: phase-detected Techniques," Radiology **215**, 286 – 293 (2000).
6. D. Paganin, S. Mayo, T. Gureyev, P. Miller, and S. Wilkins, "Simultaneous phase and amplitude extraction from a single defocused image of a homogeneous object," J. Microsc. **206**, 33 – 40 (2002).
7. S. Mayo, T. Davis, T. Gureyev, P. Miller, D. Poganin, A. Pogany, A. Stevenson, and S. Wilkins, "X-ray phase-contrast microscopy and microtomography," Opt. Express **11**, 2289 – 2302 (2003).
8. X. Wu and H. Liu, "A general theoretical formalism for X-ray phase contrast imaging," J. X-ray Sci. and Tech. **11**, 33 – 42 (2003).
9. X. Wu and H. Liu, "Clinical implementation of phase-contrast x-ray imaging: Theoretical foundations and design considerations," Med. Phys. **30**, 2169 – 2179 (2003).
10. X. Wu and H. Liu, "A new theory of phase-contrast x-ray imaging based on Wigner distributions," Med. Phys. **31**, 2378 – 2384 (2004).

11. E. Donnelly, R. Price, and D. Pickens, "Experimental validation of the Wigner distributions theory of phase-contrast imaging," Med. Phys. **32**, 928 – 931 (2005).
12. D. Zhang, M. Donvan, L. Fajardo, A. Archer, X. Wu, and H. Liu, "Preliminary feasibility study of an in-line phase contrast x-ray imaging prototype," IEEE Trans. Biomed. Eng. **55**, 2249 – 2257 (2008).
13. X. Wu, H. Liu, and A. Yan, "X-ray phase-attenuation duality and phase retrieval," Opt. Lett. **30**(4), 379 – 381 (2005).
14. X. Wu and H. Liu, "X-Ray cone-beam phase tomography formulas based on phase-attenuation duality," Opt. Express **13**, 6000 – 6014 (2005).
15. P. Cloetens, R. Mache, M. Schlenker, and S. Lerbs-Mache, "Quantitative phase tomography of Arabidopsis seeds reveals intercellular void network," PNAS **103**, 14,626 – 14,630 (2006).
16. X. Wu, H. Liu, and A. Yan, "Phase-Contrast X-Ray Tomography: Contrast Mechanism and Roles of Phase Retrieval," Eur. J. Radiology **68**, S8 – S12 (2008).
17. J. Guigay, M. Langer, R. Boistel, and P. Cloetens, "Mixed transfer function and transport of intensity approach for phase retrieval in the Fresnel region," Opt. Lett. **32**, 1617 – 1619 (2007).
18. ICRU, "Tissue Substitutes in Radiation Dosimetry and Measurement," in *Report 44 of the International Commission on Radiation Units and Measurements* (Bethesda, MD, 1989).
19. N. Dyson, *X-Rays in Atomic and Nuclear Physics* (Longman Scientific and Technical, Essex, UK, 1973).
20. T. Gureyev, Y. Nesterets, D. Paganin, A. Pogany, and S. Wilkins, "Linear algorithms for phase retrieval in the Fresnel region. 2. Partially coherent illumination," Opt. Comm. **259**, 569 – 580 (2006).
21. M. Born and E. Wolf, *Principles of Optics*, 6th ed. (Pergamon, Oxford, 1980).
22. F. Meng, H. Liu and X. Wu, "An iterative phase retrieval algorithm for in-line phase imaging," Opt. Express **15**, 8383 – 8390 (2007)
23. M. Langer, P. Cloetens, J.P. Guigay and F. Peyrin, "Quantitative comparison of direct phase retrieval in in-line phase tomography," Med. Physics **35**, 4556 – 4566 (2008)
24. A. Yan, X. Wu and H. Liu, "An attenuation-partition based iterative phase retrieval algorithm for in-line phase-contrast imaging" Opt. Express **16**, 13330 – 13341 (2008)

1. Introduction

Conventional x-ray imaging for soft tissues (such as breast, brain, liver, etc.) is limited in its sensitivity for detecting subtle tissues pathological changes, since the imaging relies on the small difference in x-ray attenuation between the lesions and soft tissues of variable structure. However, as x-ray wave passes through tissues, x-ray undergoes phase-shifts as well. The amount of x-ray phase shift ϕ by tissues is

$$\phi(\vec{r}) = -\left(\frac{hc}{E}\right) r_e \int \rho_e(\vec{r}, z) dz = -\left(\frac{hc}{E}\right) r_e \rho_{e,p}(\vec{r}), \tag{1}$$

where r_e is the classical electron radius, h is the Plank constant and c the speed of light, E is x-ray photon energy. Here ρ_e denotes tissue electron density, and the integration of electron density ρ_e is over the x-ray path and the integral is the projected electron density $\rho_{e,p}$ [1, 2, 3]. It turns out that x-ray phase-shift differences between tissue and lesions are about one thousand times larger than their attenuation differences [1, 2, 3]. Hence the phase-sensitive imaging has the potential to greatly enhance the lesion detection sensitivity and specificity, and reduce the radiation dose associated with x-ray imaging. In the inline phase contrast imaging as studied in previous works, the x-rays with shifted phases diffract from the object to the detector, and the diffracted x-rays form bright and dark fringes at tissue boundaries. The edge enhancement thus generated relies on the spatial coherence of the x-ray source, and Laplacian and gradients of x-ray phase-shifts caused by the object, and gradients of the objects attenuation [4, 5, 6, 7, 8, 9, 10, 11, 12, 13, 14]. The procedure of disentangling tissue phase-shifts from the mixed contrast mechanism and retrieving the phase maps from acquired phase contrast images is called the phase retrieval. Phase retrieval technique plays a central role in phase-sensitive x-ray imaging. By means of phase retrieval, one can reconstruct a quantitative map of phase-shifts, a phase image of the imaged object [3, 6, 13, 15, 16]. According to Eq. (1), a retrieved phase image is equivalently a map of imaged objects quantitative projected electron densities. Therefore, tissue phase images can provide quantitative tissue characterization,

which potentially can increase the sensitivity and specificity of a diagnosis. Moreover, phase retrieval is a necessary procedure for phase-sensitive volumetric imaging such as the phase-sensitive tomography and tomosynthesis [7, 14, 15]. In the phase-sensitive imaging, x-ray does NOT propagate along straight lines because of x-ray refraction and diffraction at tissue interface and boundaries. The diffraction fringes generated by phase contrast at tissue interfaces will obviously render conventional volumetric image reconstruction methods erroneous, since conventional volumetric reconstruction methods assume that x-rays propagate along straight lines. The phase-sensitive CT experiments showed that conventional tomography reconstruction algorithms applied to phase-contrast projections can lead to erroneous tomography images with artifacts such as the streaks and negative densities [7]. The exact mechanism of the phenomenon was revealed in one of our recent work. In fact, if we denote the imaged objects linear attenuation coefficient by $\mu(\vec{r})$ and its electron density by $\rho_e(\vec{r})$, with the conventional filtered backprojection method the reconstructed "apparent attenuation coefficients" $\mu_{\text{recon}}(\vec{r})$ was found as [17]:

$$\mu_{\text{recon}}(\vec{r}) = \mu(\vec{r}) - R_2 \cdot \frac{r_e \lambda^2}{2\pi} \cdot \left(\frac{\partial^2}{\partial x^2} + \frac{\partial^2}{\partial y^2} + \frac{\partial^2}{\partial z^2} \right) \rho_e + \mu_{\text{mixed}}(\vec{r}), \qquad (2)$$

where R_2 denotes the object-detector distance, λ the x-ray wavelength. Eq. (2) shows that the reconstructed tomogram consists of three sub-tomograms. The first sub-tomogram is the tomogram of the tissue linear attenuation coefficients $\mu(\vec{r})$. The second sub-tomogram is a scaled map of the 3-D Laplacian of tissue electron densities. The third sub-tomogram $\mu_{\text{mixed}}(\vec{r})$ represents the artifacts reflecting the global variation of both $\mu(\vec{r})$ and $\rho_e(\vec{r})$, but is not representing the local variations of $\mu(\vec{r})$ and $\rho_e(\vec{r})$. It is this term that causes artifacts such as the streaks in reconstruction images. In order to correctly deal with volumetric reconstruction issue, as a general strategy one should first disentangle tissue phase-shifts from the mixed contrast mechanism from acquired phase-sensitive projections and retrieve the phase maps for all projections, then reconstruct the 3D images of object attenuation coefficients and electron densities, respectively.

For phase retrieval one in general needs to acquire at least two and mostly four to five images with different object-detector distances [3, 15]. This requirement is imposed by the x-ray wave nature and its wave equation [3, 8, 9, 10]. Multiple image-acquisitions for a phase retrieval increase radiation dose associated with the technique. For phase sensitive tomography or tomosynthesis, multiple image-acquisitions for each projection-angle make phase-sensitive tomography and tomosynthesis implementation especially cumbersome: multiple phase-contrast images have to be acquired with different object-detector distances for all the projections during a scan, and the number of required projections can be as high as one thousand. In addition, the image data alignment procedure is quite time-consuming. Moreover, radiation dose is multiplied for multiple image acquisition per projection view as well. Therefore, an important challenge is to find an effective and low-dose approach for phase retrievals for phase-sensitive imaging. Many studies were conducted addressing this challenge [6, 13, 14]. We proposed a unique solution for phase-sensitive imaging with high energy x-rays. We noted that with increasing x-ray energy tissues photoelectric absorption decreases as $1/E^n$ with $n \approx 3 - 4$. but tissues phase shift decreases much slower, and only as $1/E$ as is shown in Eq. (1). Therefore, phase-sensitive imaging with x-rays can fully take advantage of phase contrast and greatly reduce radiation doses associated with x-ray imaging, by taking advantage of the dual relation between the high energy x-rays phase-shifts and attenuation for soft tissues. Furthermore, analyzing the tissue attenuation data, we observed that the soft tissue attenuation cross sections are very well approximate by that of x-ray incoherent scattering for x-rays of about 60 keV to 500 keV. Under this circumstance, we noted that soft-tissue attenuation and soft-tissue phase are all related to the projected electron density, we called this new notion as the phase-attenuation duality. Based
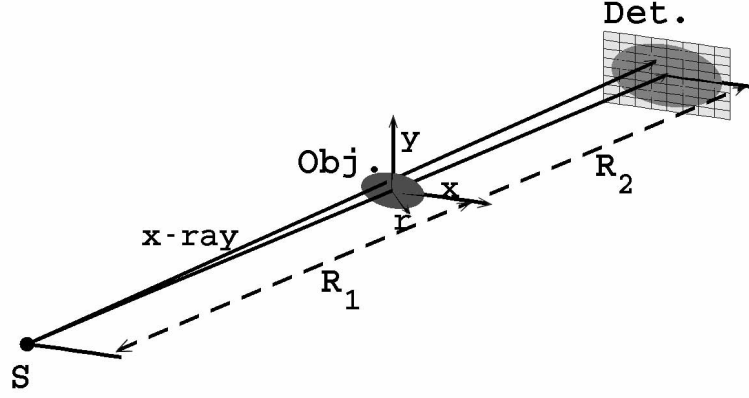
Fig. 1. A shematic diagram for the measuring system

on this concept of phase-attenuation duality, we found a way to retrieve a phase-map from only one single recorded image, that is, the retrieved phase map is given by [13]:

$$\phi(\vec{r}) = \frac{\lambda r_e}{\sigma_{\mathrm{KN}}} \ln \left\{ \left(1 - \left(\lambda^2 r_e R_2/(2\pi M \sigma_{\mathrm{KN}})\right) \nabla^2\right)^{-1} \left(\frac{M^2 I(M\vec{r}; R_1 + R_2)}{I_{\mathrm{in}}}\right)\right\}, \qquad (3)$$

where R_1 is the distance from the point x-ray source to object, R_2 is the distance from object to detector, $M = (R_1 + R_2)/R_1$ is the geometric magnification, $\vec{r}$ is the position vector (see Fig. 1.) In Eq. 3, $I(M\vec{r}; R_1 + R_2)$ is the measured image intensity at detector plane, and I_{in} is the intensity at entrance, the operator ∇^2 denotes the Laplacian operator. In Eq. (3) σ_{KN} is the Klein-Nishina total cross section, that is, the total cross section for x-ray Compton scattering with a free electron [17]. Note that σ_{KN} is x-ray energy dependent, as is shown below. We point out that the high sensitivity of x-ray phase change is realized as the high ratio $\lambda r_e/\sigma_{\mathrm{KN}} \gg 1$ in this circumstance. In fact, for clinical imaging photon energy is no higher than 150 keV, and in this case $\lambda r_e/\sigma_{\mathrm{KN}} \sim 10^3$. In other words, with this duality the high sensitivity of phase imaging manifests itself as the high ratio of x-ray wavelength over the classical electron radius. Compared to the common multiple-acquisition based phase retrieval approaches in the literature [3, 6, 15], our duality-based phase retrieval method is a conveniently implemented method with tremendous dose-saving for many potential applications such as mammography. These advantages will be critical for phase-sensitive volumetric imaging such as breast tomosynthesis and computed tomography.

However, there is a limitation on applicability of the phase retrieval formula Eq. (3). In fact. Eq. (3) is not valid for the cases with very high spatial resolution and with large object-detector distances. The physics behind this can be intuitively explained as follows. In fact, in inline phase-sensitive imaging the phase contrast is formed by the diffraction from the object to the detector of x-rays with shifted phases. The Fresnel diffraction can be thought as a x-ray wave-front filtering with the Fresnel propagator $\exp(i\pi\lambda z \vec{u}^2)$, where λ is the wavelength and $\vec{u}$ is the wave-front transverse spatial frequency vector, and $z = R_2/M$ in terms of the parameters in Eq. (3). So the phase of the propagator, i.e. $\pi\lambda z \vec{u}^2$, determines how strongly the wave-front exit from the object will be diffracted in x-ray propagation. The phase retrieval formula Eq. (3) was derived by linearizing Fresnel propagator phase under the assumption of $\pi\lambda z \vec{u}^2 \ll 1$ [8, 13]. This linearizing is equivalent to simplifying x-ray wave equation of motion to the transport of intensity of equation (TIE) [8]. However, for cases with very high spatial resolution and with

large object-detector distances, such as cases with phase-sensitive imaging experiments with synchrotron based x-ray sources, or the high resolution imaging experiments with biological specimen or small animals, the high spatial resolution or large propagation distances make Fresnel propagator phases $\pi\lambda z\vec{u}^2$ larger than 1 for many transverse spatial frequencies of x-ray wave-front. For example, for 60 keV x-rays, if $M = 1$ and $R_2 = 2$m, detector pixel is 5 μm, then $\pi\lambda z\vec{u}^2 = 1.299$. For these cases one cannot linearize Fresnel propagators and should consider the full exponential propagators instead. In section 2, we will first briefly review the concept of the phase-attenuation duality and how it greatly simplify the phase retrieval for soft-tissue objects. We will then derive a new and general PA-Duality based phase retrieval formula, as the main result of this work. With this general formula, one can retrieve the phase from one single phase contrast image and is valid for cases involved with large Fresnel propagator phases. Hence this new phase retrieval formula extends its applicability to cases with very high spatial resolution and with large object-detector distances. In section 3, we show the simulation results with the general formula for phase retrieval.

2. Phase-attenuation duality and phase retrieval from one single phase contrast image for soft tissue objects

As is explained in previous works [3, 4, 8, 9, 10], in phase-sensitive imaging the imaged object can be modeled by a two-dimensional transmission function $T(\vec{r}) = A_0(\vec{r})e^{i\phi_0(\vec{r})}$, where $\phi_0(\vec{r})$ denotes the x-ray phase-shift caused by the object, and $A_0(\vec{r})$ denotes the x-ray transmission, or the attenuation-map of object. For sake of clarity in exploring the effects of non-linearity of the Fresnel propagators, we assume the x-ray source is a quasi-monochromatic point source in following derivations. We will discuss more general x-ray sources in section 3.

Let R_1 denote the source-object distance and R_2 the object-detector distance. The geometric magnification factor M is equal to $(R_1 + R_2)/R_1$. We also assume that one encounters only moderate variation of the object phase function $\phi(\vec{r})$ such that $|\phi(\vec{r} + \lambda R_2\vec{u}/2M) - \phi(\vec{r} - \lambda R_2\vec{u}/2M)| \ll 1$ [3]. Transmitting from the object, x-rays undergo attenuation and phase-shift, and diffract over a distance R_2 to the detector. An important task is to find out the formula of the image intensity as function of the objects transmission function and imaging geometry. A general solution had been found in one of our previous works [3]. Starting from the paraxial Fresnel-Kirchhoff diffraction theory, we found out in this work that the Fourier transform of x-ray irradiance at detector plane is given by:

$$\hat{\mathscr{F}}(I(\vec{r}_D)) = \frac{I_{\text{in}}}{M^2}\left\{\cos\left(\frac{\pi\lambda R_2\vec{u}^2}{M}\right)\left(\hat{\mathscr{F}}(A_0^2) - i\frac{\lambda R_2}{M}\vec{u}\cdot\hat{\mathscr{F}}(\phi\nabla A_0^2)\right) + \right.$$
$$\left. + 2\sin\left(\frac{\pi\lambda R_2\vec{u}^2}{M}\right)\left(\hat{\mathscr{F}}(A_0^2\phi) + i\frac{\lambda R_2}{4M}\vec{u}\cdot\hat{\mathscr{F}}(\nabla A_0^2)\right)\right\}, \quad (4)$$

where $I(\vec{r}_D)$ denotes the x-ray irradiance at the detector entrance, and the symbol $\hat{\mathscr{F}}(\cdot)$ denotes the 2-D Fourier transform and I_{in} is the intensity of the incident x-ray upon the object, and $\vec{u}$ is the spatial frequency vector in the object plane. Note that the Fresnel propagator phases $\pi\lambda R_2\vec{u}^2/M$ enter Eq. (4) as the argument of sinusoidal transfer functions. For cases with moderate spatial resolutions $\vec{u}$ and R_2, Eq. (4) is much simplified, and the inverse Fourier transformation of the simplified Eq. (4) can be written as [8]:

$$I(\vec{r}; R_1 + R_2) = \frac{I_{\text{in}}}{M^2}\left\{A_0^2\left(\frac{\vec{r}}{M}\right) - \frac{\lambda R_2}{2\pi M}\nabla\cdot\left(A_0^2\nabla\phi\left(\frac{\vec{r}}{M}\right)\right)\right\}. \quad (5)$$

Equation (5) is the TIE-based formula for image irradiance, which was first derived by Nugent and colleagues[3]. Recently Guigay et al showed the limitations of Eq. (5) with theoretical

analysis and experiments [17]. They found that for in-line phase-sensitive imaging with long R_2 and high resolutions such that $\pi \lambda R_2 \vec{u}^2/M > 1$, the phase retrieval based on Eq. (5) would be inaccurate, one has to use the general formula Eq. (4) for accurate quantitative phase imaging.

Furthermore, we note that soft tissues encountered in clinical imaging are composed almost exclusively by atoms of the light elements with the atomic numbers $Z < 10$. For example, the composition of breast tissue consists mainly of light elements such as hydrogen, carbon, nitrogen and oxygen. In contrast, the sum of weight fractions of other heavier elements in breast tissue is only less than 1% [18]. The same is true for other soft tissues such as the brain grey/white matter [18]. Analyzing the tissue attenuation data, we observed that the soft tissue attenuation cross sections are very well approximated by that of x-ray incoherent scattering for x-rays of about 60keV to 500keV[19]. In addition, the incoherent scattering functions become linearized as well [19]. Under this circumstance, while the phase-shift is caused by the coherent x-ray scattering, but soft tissue attenuation is determined by the incoherent x-ray scattering for soft tissues, so both the x-ray phase-shift and attenuation by soft tissues are all determined by the projected electron density for these high energy x-rays. We called this complementary relationship between phase-shift and attenuation for soft tissues as the phase-attenuation duality. When the P-A duality holds, x-ray attenuation and phase shift by the object is related in following way:

$$\phi(\vec{r}) = -\lambda r_e \rho_{e,p}(\vec{r}), \qquad A_0^2(\vec{r}) = \exp(-\sigma_{\mathrm{KN}} \rho_{e,p}(\vec{r})), \qquad (6)$$

where σ_{KN} is the total cross section for x-ray Compton scattering with a free electron:

$$\sigma_{\mathrm{KN}} = 2\pi r_e^2 \left\{ \frac{1+\eta}{\eta^2} \left[\frac{2(1+\eta)}{1+2\eta} - \frac{1}{\eta} \ln(1+2\eta) \right] + \frac{1}{2\eta} \ln(1+2\eta) - \frac{1+3\eta}{(1+2\eta)^2} \right\}, \qquad (7)$$

where $\eta = E_{\mathrm{photon}}/m_e c^2$, here we denote the photon energy of the primary x-ray beam by E_{photon}, and $m_e c^2$ is the rest electron energy and equal to 511keV. The duality condition can be used to simplify Eq. (4). In fact, we can rewrite Eq. (4) as

$$\hat{\mathscr{F}}(I(\vec{r}_D)) = \frac{I_{\mathrm{in}}}{M^2} \left\{ \cos\left(\frac{\pi \lambda R_2 \vec{u}^2}{M}\right) \left[\hat{\mathscr{F}}(A_0^2) - \frac{\lambda R_2}{2\pi M} \hat{\mathscr{F}}(\nabla \cdot (A_0^2 \nabla \phi)) \right] + \right.$$
$$+ 2 \left[\sin\left(\frac{\pi \lambda R_2 \vec{u}^2}{M}\right) - \frac{\pi \lambda R_2 \vec{u}^2}{M} \cos\left(\frac{\pi \lambda R_2 \vec{u}^2}{M}\right) \right] \hat{\mathscr{F}}(A_0^2 \phi) -$$
$$\left. - \frac{\lambda R_2}{4\pi M} \sin\left(\frac{\pi \lambda R_2 \vec{u}^2}{M}\right) \hat{\mathscr{F}}(\nabla^2 A_0^2) \right\}. \qquad (8)$$

Especially with the duality condition we found

$$\hat{\mathscr{F}}(\nabla \cdot (A_0^2 \nabla \phi)) = \left(-4\pi^2 \vec{u}^2\right) \left(\frac{\lambda r_e}{\sigma_{\mathrm{KN}}}\right) \cdot \hat{\mathscr{F}}(A_0^2),$$
$$\hat{\mathscr{F}}(A_0^2 \phi) = \lambda r_e \hat{\mathscr{F}}\left(\frac{\partial A_0^2}{\partial \sigma_{\mathrm{KN}}}\right) \approx \frac{\lambda r_e}{\sigma_{\mathrm{KN}}} \hat{\mathscr{F}}(A_0^2 - 1). \qquad (9)$$

In Eq. (9) we made an approximation of dropping the negligible contribution of the higher order terms of $\sigma_{\mathrm{KN}}/\lambda r_e$. The approximation is based on $\sigma_{\mathrm{KN}}/\lambda r_e \approx 10^{-3}$, and we assumed $|\phi(\vec{r} + \lambda R_2 \vec{u}/2M) - \phi(\vec{r} - \lambda R_2 \vec{u}/2M)| \ll 1$, moderate variations of object phase shifts. Substituting Eqs. (9) into Eq. (8), we found:

$$\hat{\mathscr{F}}\left(\frac{M^2 I(\vec{r}_D)}{I_{\mathrm{in}}}\right) \approx \left[\cos\left(\frac{\pi \lambda R_2 \vec{u}^2}{M}\right) + \left(2\frac{\lambda r_e}{\sigma_{\mathrm{KN}}} + \frac{\pi \lambda R_2 \vec{u}^2}{M}\right) \sin\left(\frac{\pi \lambda R_2 \vec{u}^2}{M}\right) \right] \cdot \hat{\mathscr{F}}(A_0^2). \qquad (10)$$

Equation (10) is the central result of this work, it is the formula for x-ray irradiance for high resolution soft tissue imaging with high energy x-rays. In the derivation the parameter $\lambda r_e/\sigma_{\mathrm{KN}}$

plays a significant role. It is interesting to note that Gureyev et al obtained a similar result in ref.[20] (Eq.(24)) with the exception that the term $\pi\lambda R_2\vec{u}^2/M$ in Eq. (10) was absent. The differences may lie in the different assumptions made regarding the object transmission functions and x-ray energies. Gureyev and coauthors assumed the objects as single material homogeneous objects [20], but our results are for heterogeneous objects of the light elements imaged with high energy x-rays (60 keV or higher), i.e., for the cases the phase-attenuation duality holds. In addition, in their derivation they separated the slowly and rapidly varying components of the amplitude and phase, and they assumed that the magnitude of the rapidly varying components are much smaller than 1, but we did not make such limiting assumption in derivation of Eq. (10). We stress that the Klein-Nishina cross-section is energy dependent shown in Eq. (7) and $\lambda r_e/\sigma_{\text{KN}}$ is about 1000 for inline x-ray energy range used in diagnostic imaging. This large $\lambda r_e/\sigma_{\text{KN}}$ represents the high sensitivity of phase contrast in tissue differentiation, but it also makes the x-ray irradiance formula Eq. (10) getting very much simplified. It is easy to verify that for the low resolution cases such as those with $\pi\lambda R_2\vec{u}^2/M \ll 1$, Eq. (10) is reduced to

$$\hat{\mathscr{F}}\left(\frac{M^2 I(\vec{r}_D)}{I_{\text{in}}}\right) = \left(1 + 2\left(\frac{\lambda r_e}{\sigma_{\text{KN}}}\right)\left(\frac{\pi\lambda R_2\vec{u}^2}{M}\right)\right) \cdot \hat{\mathscr{F}}\left(A_0^2\right), \tag{11}$$

we recover our previous result as shown in [13]. On the other hand, for general cases $\pi\lambda R_2\vec{u}^2/M \sim 1$ or $\pi\lambda R_2\vec{u}^2/M > 1$ Eq. (11) cannot be applied, and one should use Eq. (10) for phase retrieval as is shown below.

3. Simulation results

Comparing Eq. (10) and Eq. (11) for use in performing phase retrieval, the only difference lies in the inverse filters derived for retrieving $\hat{\mathscr{F}}\left(A_0^2\right)$. For phase retrieval based on Eq. (10) the inverse filter is found as

$$\frac{1}{\cos(\alpha) + (2\gamma + \alpha)\sin(\alpha)} = \frac{1}{\delta \cdot \cos(\alpha_1)}, \tag{12}$$

where $\alpha = \pi\lambda R_2\vec{u}^2/M$, the FT-space Fresnel Propagator phase as defined in section 1, and $\gamma = \lambda r_e/\sigma_{\text{KN}}$, which represents the phase contrast enhancement as explained earlier. $\delta = \sqrt{1 + (2\gamma + \alpha)^2}$ and $\alpha_1 = \alpha - \sin^{-1}[(2\gamma + \alpha)/\delta]$. On the other hand, for phase retrieval based on Eq. (11) the inverse filter will be

$$\frac{1}{1 + 2\gamma\alpha}. \tag{13}$$

Since $\gamma \sim 10^3$, the filters in Eq. (12) and Eq. (13) are close when α is small. When α is getting bigger, close to or greater than π (α_1 close to $\pi/2$), the difference between the two inverse filters is getting bigger. Figure 2 shows a plot of the two filters, with respect to the change of α. The inverse filter in Eq. (12), depicted in Fig. 2 as the solid line, changes the sign when α passes through $k\pi$ (and thus α_1 passes through $(k-1/2)\pi$) and diverges to ∞ when $\alpha_1 = (k-1/2)\pi$, $k = 1, 2, \cdots$. On the other hand, the filter in Eq. (13), depicted as the dashed line in Fig. 2, keeps positive and approaches zero as α gets bigger. So the difference of the retrieved phase maps using Eq. (10) and Eq. (11) will be highly dependent on the value of the Fresnel propagator phase $\alpha = \pi\lambda R_2\vec{u}^2/M$.

To demonstrate this phenomenon, we performed two simulations. First, we set the phase shift ϕ to be a sine-function in x direction with period of 32 pixel size and constant in y direction. Assuming the pixel pitch is p μm, the spatial frequency corresponding to ϕ, in x direction, is $\mu_{x0} = 1/32p$ 1/μm. In our simulations, for the purpose of simplification, the magnification M as well as the intensity at entrance, I_{in}, are assumed to be 1. The x-ray photon energy is set
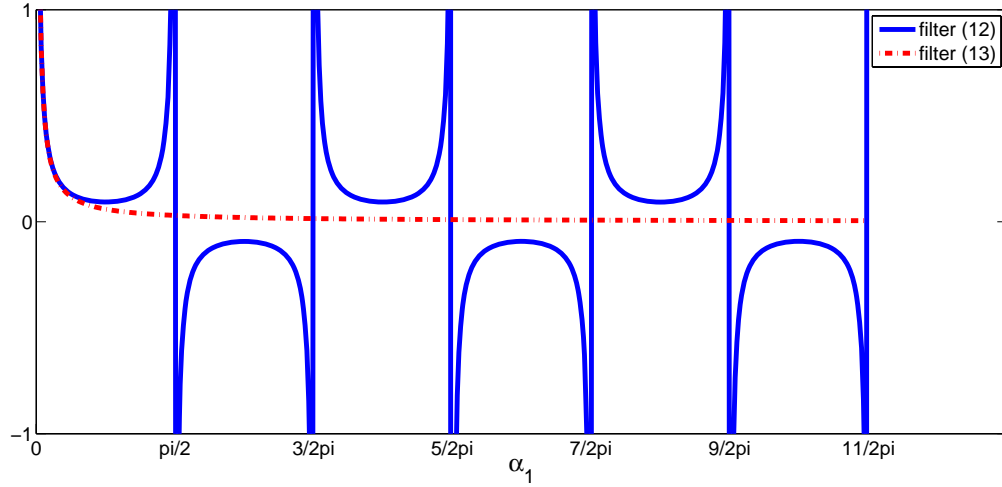
Fig. 2. Plots of filters (13) and (12)

to 60 keV. This gives the x-ray wavelength $\lambda = 2.0667 \times 10^{-11}$ m and the total cross section for x-ray Compton scattering with a free electron $\sigma_{KN} = 5.4526 \times 10^{-29}$ m^2 as determined from Eq. (7). The classical electron radius r_e is set to 2.82×10^{-15} m. By assuming the detectors resolution $p = 1$ μm and the phase shift $\phi(x,y) = 0.5\sin(32px) - 1$, according to the phase-attenuation duality discussed earlier, the attenuation map is related to the phase map as $A_0^2(x,y) = \exp[\sigma_{KN}/\lambda r_e \cdot \phi] = \exp[(\sin(32px) - 2)/2\gamma]$, with $\gamma = \lambda r_e/\sigma_{KN} = 1.0726 \times 10^3$. We then performed Fresnel diffraction to determine the phase-contrast image irradiances at distances downstream[21], and the retrieved maps of A_0^2 were found by using the inverse filters of Eq. (12) and Eq. (13), which were derived based on Eq. (10) and Eq. (11), respectively. Because of the large value of γ, phase contrast image irradiances $\{I\}$ were found be maps with each I being dominated by two single frequency component at $u_x = \pm u_{x0}$ ($u_{x0} = 1/32p = 1/32 \times 10^6$ m) plus a zero frequency component. This being so, the shape and variation of the retrieved A_0^2-maps were determined by their dominant frequency component at frequencies $u_x = \pm u_{x0}$. In order to clearly show the differences between phase retrievals based on Eq. (10) and Eq. (11), we examined the ratio of the dominant frequency components of the two retrieved A_0^2-maps based on Eq. (10) and Eq. (11), respectively. We found the ratio being $r = (1 + 2\gamma\alpha)/(\delta \cdot \cos(\alpha_1))$ for a given object-detector distance R_2. This ratio reflects the capability of achieving accurate phase retrieval with Eq. (10) against Eq. (11). For small $\alpha \ll 1$, that is, for small Fresnel propagator phases, this ratio is 1, so Eq. (10) against Eq. (11) both are equally good for the accurate phase retrieval. However, when α is chosen such that $\cos(\alpha_1)$ is close to 0, this ratio can be very large. For example by setting $R_2 = 49.55$ m, we have α mentioned above equals to π, the ratio $r = (1 + 2\gamma)/(\delta \cdot \cos(\alpha_1)) \approx 6700$. This large ratio means that the retrieved A_0^2-map based on Eq. (11) has diminished image-contrast and erronous values, as is shown in Fig.3(c). The phase retrieval result based on Eq. (10), shown in Fig. 3(d), however is much more accurate. When $R_2 = 49.55$ m, the FT-space Fresnel Propagator phase $\alpha = \pi\lambda R_2 \vec{u}^2/M \approx \pi$. So we have, from Eq. (10), $\hat{\mathscr{F}}((M^2/I_{in})I) \approx -\hat{\mathscr{F}}(A_0^2)$, which is different from the result $\hat{\mathscr{F}}((M^2/I_{in})I) \approx [1 + 2\pi(\lambda r_e/\sigma_{KN})]\hat{\mathscr{F}}(A_0^2)$ derived from the conventional TIE prediction (Eq. (11)), which does not hold for such large Fresnel Propagator phases. This phenomenon is shown in Fig. (3)(b), where the intensity I is acquired with Fresnel diffraction,

in which the dark-white area in A_0^2 is reversed. Note that the inverse filter in Eq. (12) is singular at $\alpha_1 = (k - 1/2)\pi$, $k = 1, 2, \cdots$, because of the zero-crossing of $\cos(\alpha_1)$. To deal with the singularity associated with the zero-crossing of $\cos(\alpha_1)$, one should regularize the inverse filter. A common regularization technique is the Tikhonov regularization, which modifies $1/\cos(\alpha_1)$ in the filter of Eq. (12) to $\cos(\alpha_1)/(\cos(\alpha_1)^2 + \kappa^2)$, where κ is the Tikhonov regularization parameter. In this specific example of the sinusoidal object, however, since we know $\hat{\mathscr{F}}(I)$ is dominated by frequency-components only at $u_x = \pm u_{x0}$ and $(u, v) = (0, 0)$, by setting $\hat{\mathscr{F}}(I) = 0$ at all other frequency points purposely, we can avoid the problem caused by the zero-crossing of the inverse filter.
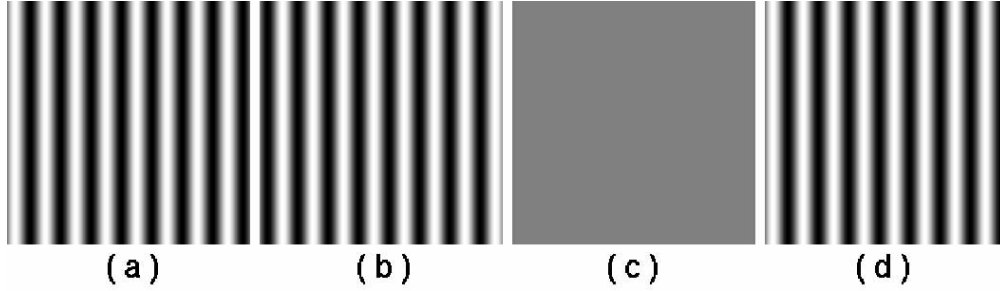

Fig. 3. Comparison of the quality of the retrieved results A_0^2 using Eq. (11) and Eq. (10). $A_0^2 = \exp[\phi/\gamma]$, where phase shift $\phi = 0.5\sin(32px) - 1$, pixel pitch $p = 1\mu m$, and object to detector distance $R_2 = 49.55$m. (a) is the true A_0^2; (b) is the phase-contrast intensity image I acquired from Fresnel diffraction; (c) is retrieved A_0^2 using Eq. (11); (d) is retrieved A_0^2 using Eq. (10).

In another simulation, we set all the parameters the same as the previous simulation except replacing the test-object with the well-known Lena image as is shown in Fig. 4(a). The simulation results for the case of $R_2 = 5$ m are shown in Figures 4(c)-4(d). The phase-contrast image I, shown in Fig. 4(b), is acquired with Fresnel diffraction from the object downstream to the detector [21]. Figure 4(c) shows the retrieved image with the inverse filter of Eq. (13), which is based on Eq. (11). Since the filter of Eq. (13) is incorrect when the Fresnel propagator phase α is big, say close or greater than π, the high frequency components of the object was unduly suppressed in the phase-retrieval. This deficiency is reflected in Fig. 4(c) such that the retrieved image gets blurred in locations with high contrast changes, such as the hair, the edge of the hat and body. In contrast, the phase retrieval using the inverse filter of Eq. (12), which is based on Eq. (10), preserves objects high frequency components, as is shown in Fig. 4(d).

As stated above, a regularization must be used to overcome the difficulty associated with the zero-crossing in the denominator of inverse filter in Eq. (13). The zero-crossing occurs obviously at $\alpha_1 = (k - 1/2)\pi$, $k = 1, 2, \cdots$. The Tikhonov regularization would replace $1/\cos(\alpha_1)$ in the inverse filter of Eq. (13) by the following

$$\frac{\cos(\alpha_1)}{\cos(\alpha_2)^2 + \kappa^2}, \tag{14}$$

where κ is a small constant. However, this form of regularization is not optimal since it will deviate from the original inverse filter when α_1 is small. In other words, the test-object's low frequency components would not be fully reconstructed in the retrieval. In order to get around this drawback, we note that the zero-crossing occurs only when α_1 is close or greater than $\pi/2$, while the most low frequency components have $\alpha < 1$. Hence we set the regularization parameter $\kappa = 0$ when α is less than some threshold value α_0, and $\kappa > 0$ when α is greater than
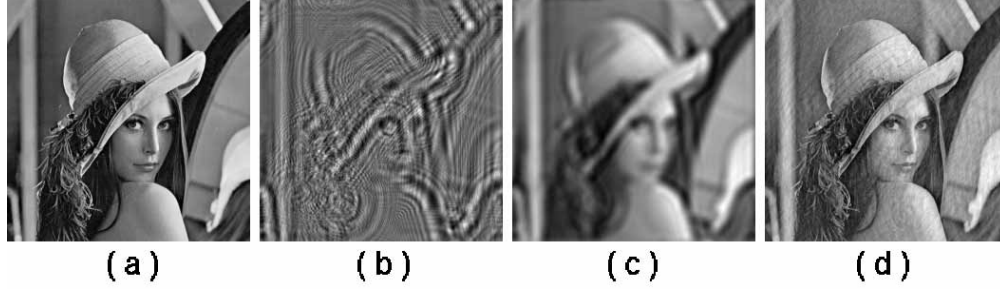
Fig. 4. Comparation of the retrieved results using Eq. (11) and Eq. (10) with $R_2 = 5$m. (a) is the true A_0^2; (b) is the phase-contrast image I acquired from Fresnel diffraction; (c) is retrieved using Eq. (11); (d) is retrieved using Eq. (10).

α_0. In our simulation, we set this threshold $\alpha_0 = 0.8$, so $\kappa = 0$ when $\alpha < 0.8$, and $\kappa = 0.12$ when $\alpha > 0.8$. We can see from the image in Fig. 4(c) that most of the low frequency information is preserved. On the other hand, the quality of the results can also be numerically determined by computing the error comparing to the true A_0^2 image. By taking the L_2-measure, which is defined as the integrated squared errors, we have the absolute errors for methods (10) and (11) being 0.014 and 0.021 respectively.

4. Conclusions

Phase retrieval is required for achieving artifact-free x-ray phase-sensitive 3D imaging. Multiple image-acquisitions per projection are required in general for phase retrieval [3, 4, 15, 17, 22, 23, 24]. This requirement impedes the implement of x-ray phase-sensitive 3D imaging, especially for phase-sensitive 3D imaging in clinical applications. A phase-retrieval approach based on the phase-attenuation duality with high energy x-rays can greatly facilitate for phase sensitive imaging by allowing phase retrieval from only one single projection image. However, the previously derived phase retrieval formula is valid only for small Fresnel propagator phases corresponding to common clinical imaging tasks. In this work we generalized the previous phase retrieval formula to Eq. (10), which can be applied for cases with large Fresnel propagator phases corresponding to high spatial resolution imaging. The computer simulation demonstrated superiority of this new formula over the previous duality-based phase-retrieval formula in reconstructing the high frequency components of imaged objects. In addition, a modified Tikhonov regularization technique has been devised for phase retrieval in cases of very high resolution and large object-detector distance such that some Fresnel propagator phases may be close or greater than π. This new phase retrieval formula of Eq. (10) lays the foundation for implementing high-resolution phase-sensitive 3D imaging of soft tissue objects.

Acknowledgements

5 paraspinal SBRT patients. Prescription dose to the PTV is 24Gy while constraining the cord maximum dose to 14Gy. Plan evaluation statistics include PTV V22.8Gy, PTV D95%, cord mean dose, and total beam-on time. **Results:** Collimator rotation in the five Coll-VMAT plans ranges from 26°-54°, with a median of 40°. Patient-averaged PTV V22.8Gy (94.6% with Coll-VMAT vs 92.1% VMAT and 93.3% IMRT) and D95% (22.5Gy vs 21.4Gy and 22Gy) are higher, while cord mean dose is lower (9.8Gy vs 10.0Gy and 11.7Gy). Total beam-on time is comparable to standard VMAT and substantially lower than IMRT (5164MU vs 4868MU and 13,283MU). **Conclusion:** The dosimetric advantage of Coll-VMAT is significant especially for small targets. Collimator trajectory optimization provides an additional degree of freedom in VMAT optimization that can improve dosimetric quality of paraspinal SBRT compared to standard VMAT and IMRT. **Conflict of Interest:** Research agreement with Varian Corporation

WE-E-BRB-07

Quality Assurance of Proton Range Compensators by CT Scanning
Y Zheng[1] *, E Klein[1] , D Low[1] , (1) Washington University School of Medicine, St. Louis, MO

Purpose: Patient specific range compensators (RCs) are required in passively scattered proton therapy. Conventionally, quality assurance (QA) of RC is performed by either a visual inspection or spot check of thicknesses for some drill points (e.g. 4). A more comprehensive QA of RCs is needed for precise delivery of proton beams. The purpose of this study was to develop a QA procedure by use of computed tomography (CT). **Method and Materials:** For the procedure, one or more range compensators would be scanned with a CT scanner. Software was developed to automatically segment the range compensator on CT images and calculate the thickness matrix for the RC. The CT-scanned RC thickness matrix was then compared to the expected one, which was reconstructed from the DICOM ION Radiotherapy Plan exported from a proton treatment planning system. The actual milling tool size and shape were taken into account when the RC was reconstructed. The scanned RC thickness matrix was automatically aligned to the planned RC matrix. In addition to comparing the physical thickness of the RC, we also verified the water equivalence thickness of the range compensator based on the CT scan. This would allow us to detect possible impurities or other defects of the RC. As part of the validation, we tested not only an unaltered RC, but RC that was damaged or altered post-construction. **Results:** We developed software to process the scanned CT images of the RC and reconstruct the planned RC from the radiation therapy treatment plan. We compared both the physical thickness and water equivalent thickness between the scanned RC and planned RC to quality assurance the manufacturing of the RC. Our process was able to detect deviations of less than 2 mm. **Conclusion:** We have developed a procedure to efficiently and comprehensively QA the RC.

WE-E-BRB-08

Motion and Delivery Management with Novel 4D-Optimization
O Nohadani[1] *, J Seco[2] , T Bortfeld[3] , (1) Massachusetts General Hospital, Boston, MA, (2) Mass General Hospital; Harvard Medical, Boston , MA, (3) Massachusetts General Hospital, Boston, MA

Purpose: Intensity modulated radiation therapy (IMRT) has the ability to deliver highly conformal dose distributions to tumors of complex shapes. However, motion uncertainties can substantially degrade the quality of an otherwise optimized treatment plan. We present a novel 4D-optimization technique that exploits time effects and provides plans which are robust against tumor motion and warrant deliverability. **Method and Materials**: Our 4D-optimization technique takes all registered breathing phases into account. All 4D CT data are conformally registered. To account for lung tissue inhomogeneities, we use Monte Carlo dose calculations. The 4D-optimization method seeks to minimize the overall dose subject to i) lower bounds for tumor voxels and ii) upper bounds for remaining voxels, and iii) closeness of the beamlet intensities for neighboring phases. **Results**: Based on a clinical lung cancer case, our 4D-optimization method delivers robust plans that significantly outperform the gating-based optimal plans both in terms of target coverage as well as OAR sparing. In fact, the EUD to the PTV deviates only by 0.1% from the prescribed dose for our 4D method, whereas the gated EUD deviates by 2%. Moreover, since the 4D-robust plan is quasi-static and can be delivered over all breathing phases, it warrants for a reduction in delivery errors and is less sensitive to motion uncertainties. Note that gating is quite sensitive to the choice of the gated phase and, thus, requires enlarged margins. Furthermore, due to reduced number of segments needed, we report an increase in delivery efficiency. **Conclusion**: Our proposed 4D optimization method delivers plans that are robust against motion uncertainties. Moreover, the plan is also inherently robust against sequencing and delivery errors. Therefore, it allows to reduce margins on the ITV. The method outperforms gating both in dose coverage as well as delivery robustness and increases the delivery efficiency.

Joint Imaging/Therapy Symposium
Room 303A
Image Guided Interventions: Imaging Guidance and New Technologies for Interventional Procedures

WE-E-303A-01

Image-Guided Therapies: Advances in Imaging, Modeling, and New Applications
J Siewerdsen[1] *, D Hawkes[2] *, P Keall[3] *, (1) University Health Network, Toronto, ON, CA, (2) University College London, London, GB, (3) Stanford University Cancer Center, Stanford, CA

Recent advances in imaging technology, image modeling and registration, and advanced therapeutics offer the potential for precise, image-guided therapies that will transform existing approaches to planning, intervention, adaptation, and monitoring of therapeutic response. Such therapies are marked by a dramatic increase in the application of image information from multiple modalities and demand accurate coregistration of morphological and functional information across a broad range of spatial and temporal scales. The scope of advanced therapeutic modalities enabled by such advances is broad, ranging from high-precision image-guided radiation therapy and surgery to minimally invasive target ablation, cell-based therapies, and other forms of novel therapeutics. Moreover, the information acquired during the course of intervention will drive patterns of therapy delivery that are increasingly adaptive and patient-specific. This symposium focuses on the scientific principles and recent advances in imaging, guidance, image modeling, registration, adaptation, and advanced therapy delivery techniques. Three speakers will present on topics central to such advancement: Dr. Siewerdsen will discuss principles of imaging performance, guidance, and the development and integration of new technologies for therapy guidance; Dr. Hawkes will address principles of rigid and deformable image registration, fusion, visualization, and augmented reality; finally, Dr. Keall will discuss the latest advances in imaging, adaptation, and novel treatment delivery techniques in image-guided radiation therapy.

Learning Objectives:
1. Gain exposure to new developments in imaging technologies for image-guided interventions.
2. Understand challenges in rigid and deformable image registration, fusion, and visualization.
3. Learn the latest advances in imaging, adaptation, and therapy delivery techniques in IGRT.

Imaging Scientific Session
Room 304A
New Technology, Techniques and Observer Performance

WE-E-304A-01

Contrast Mechanism and Origin of Artifacts in Phase-Sensitive X-Ray Volumetric Imaging
X Wu[1] *, A Yan[1] , H Liu[2] , (1) Univ Alabama Birmingham, Birmingham, AL, (2) Univ Oklahoma, Norman, OK

Purpose: Phase-sensitive x-ray volumetric imaging has great potential for tissue contrast enhancement and radiation dose reduction, compared to conventional tissue-attenuation based x-ray volumetric imaging. In order to achieve quantitative and artifact-free phase sensitive volumetric imaging, one should quantify the formed phase contrast and find the origin of artifacts formed in phase-sensitive volumetric imaging.

Method and Materials: We incorporated x-ray Fresnel diffraction into x-ray projection acquisitions, and reconstructed volumetric images from these phase-sensitive projections by the filtered backprojection method. A formula for the reconstructed tissue's apparent attenuation coefficients was derived for quantitative analysis.   Computer simulations of phase sensitive 3D tomography were performed, and reconstructed 3D phantom tomograms were analyzed, and the artifacts associated with phase-contrast were identified.   In order to eliminate these artifacts, we performed phase retrievals based on the phase-attenuation duality method for each projection, and these phase-retrieved projections were then used for new 3D tomographic reconstructions. **Results:** The apparent linear attenuation coefficients in 3D tomograms were found each being the sum of three parts: the tissue linear attenuation coefficient, the scaled 3D Laplacian of tissue refraction index, and the artifact depending on global distributions of tissue attenuation coefficients and refraction indices. The simulated high-resolution 3D images of phantoms exhibit severe artifacts as the upward and downward density over-shootings and the streaks. The phase retrieval was shown very effective for removing these artifacts and accurately reconstructing tissue attenuation coefficients in phase-sensitive 3D tomography. **Conclusion:** We clarified the contrast mechanism in phase-sensitive volumetric imaging, found the quantitative contribution of the phase contrast in reconstructed 3D images, and revealed the origin of severe artifacts. The need of the phase-retrievals for quantitative and artifact-free phase sensitive volumetric imaging was clearly demonstrated.

WE-E-304A-02

Development of Low Dose X-Ray Phase Contrast CT Using a Novel Projection Retrieval Reconstruction Algorithm
B Fahimian[1] *, P Cloetens[2] , Y Mao[1] , E Lee[1] , J DeMarco [1] , M McNitt-Gray[1], J Miao[1]*, (1) University of California, Los Angeles, CA, (2) European Synchrotron Radiation Facility, Grenoble, FR

Purpose: In contrast to attenuation based x-ray imaging, phase contrast x-ray imaging, produces radically enhanced images of soft tissues through imaging of the phase shift cross-section, which is 100-1000 larger than the corresponding x-ray attenuation cross-section. One obstacle in the development of phase contrast x-ray CT (PCXCT) for medical imaging is the radiation dose imparted to the patient due to large number of projections and flux required for an adequate image quality. Here we develop and quantify a methodology for low dose PCXCT using novel iterative Fourier based projection retrieval reconstruction algorithm that aims to solve the reconstruction problem from a limited number of projections through the use physical and mathematical constraints as well as the oversampling method. **Materials and Methods:** An image quality phantom, containing multiple contrast visibility and resolution inserts, was imaged at the European Synchrotron Radiation Facility (ESRF). Conventional reconstructions were produced via Filtered Back Projection (FBP) using the full set of 200 projections. Reconstructions using the projection retrieval algorithm were made with 50-60% fewer projections. The image quality of the reconstructions were quantitatively compared using SNR, CNR, and resolution. **Results:** With 60% fewer projections, the methodology matched the resolution of the FBP reconstruction, exceeded the SNR of the FBP by factor of 1.8, and exceeded the CNR of the FBP by factor of 1.7. No geometric deformations were observed due to the undersampling of the number of projections. **Conclusions:** The results indicate that the developed algorithm can reproduce reconstructions of same or superior quality using 50-60% fewer projections and hence radiation dose than FBP. **Conflict of Interest:** A portion of this research was sponsored by TomoSoft Technologies, LLC.

WE-E-304A-03

An Energy-Dispersive Technique to Measure Tissue X-Ray Coherent Scattering Form Factors
B King[1] *, P Johns[1] , (1) Carleton University, Ottawa, ON, CA

Purpose: Data for the x-ray scattering properties of tissues are needed for the development of x-ray scatter imaging systems. Published amorphous material form factors from x-ray diffractometer measurements vary significantly. An energy-dispersive technique was developed to provide more accurate measurements. **Method and Materials:** The form factor is measured as a function of the momentum transfer argument $x = \lambda^{-1}\sin(\theta/2)$ where λ is the photon wavelength and θ is the scattering angle.

Crystallographic diffractometers measure scattering versus θ at one wavelength (energy). Our method fixes θ and measures versus energy, using a high purity germanium spectrometer to measure the scattered polychromatic spectrum from a tungsten anode x-ray tube. The target is moved laterally to measure the transmitted and scattered spectra without adjusting the x-ray tube and detector. By taking the scatter to transmitted ratio bin-to-bin, the coherent scattering form factor is determined without adjustable parameters. Repeating with four θ values, the range 0.5 nm^{-1} < $x < 12$ nm^{-1} is obtained. **Results:** Measurements of the coherent scattering form factor of water and several plastics with our prototype system give good agreement for $x > 7$ nm^{-1} with the Independent Atom Model. This, together with general agreement at smaller x with published diffractometer data, is strong evidence that our measurement is accurate. The precision of our measurement has been thoroughly characterized and is approximately 10%. **Conclusion:** The energy-dispersive technique measures over a wider x range than do diffractometers and does not require the use of arbitrary scaling constants. Our measurements are limited to $5 - 10\%$ in x resolution at small θ but this is acceptable for tissue measurements. Resolution and precision will be improved by using rectangular apertures. Due to the advantages of the technique and to its thorough characterization, we expect the energy-dispersive technique to provide definitive form factor results.

WE-E-304A-04

Local Determination of Tissue Optical Properties: Reconstruction Based On Fiber-Array Reflectance Profiles
C Sheng[1] *, C Bonnerup[2] , C Austerlitz[1] , R Allison[1] , C Sibata[1] ,
(1) Department of Radiation Oncology, East Carolina University, Greenville, NC, (2) Department of Physics, East Carolina University, Greenville, NC

Quantitative evaluation of *in vivo* local tissue optical properties including scattering coefficient (μ_s), absorption coefficient (μ_a) and anisotropy (g) is often important in both photodiagnosis and phototherapy. In this study, a reflectance based fast technique was developed to determine the optical properties of turbid media using a linear-array fiber bundle probe. Five 200 um collection fibers were linearly set along from the 200 um illumination fiber with center-to-center separation of 350 um. Spatial reflectance values were sequentially measured by spectrometer connected to a fiber-switch. A model that relates the reflectance profiles to optical properties of a turbid medium was developed based on Monte Carlo simulations and phantom experiments. Simulation results at wavelength of 633 nm showed that μ_s' (2~40 cm-1) and μ_a (0~5 cm-1) can be determined by reflectance spatial profiles. Intralipid and Nigrosin were used to simulate different reduced scattering coefficient (μ_s') and absorption coefficient (μ_a) values within the same range as Monte Carlo simulation. Preliminary results show good correlation between known optical properties in tissue phantom and the measured optical properties, the average error for μ_s' and μ_a was 7.8% and 6.6%, respectively. With same reduced scattering coefficient (μ_s'), changes in the absorption coefficient (μ_a) could be measured within 0.1 cm-1. Accurate extraction of tissue optical properties from *in vivo* measurements could have potential application in noninvasively superficial (pre)cancer detection and phototherapy planning.

WE-E-304A-05

Acoustic Droplet Vaporization for Enhancement of High Intensity Focused Ultrasound Thermal Ablation
M Zhang*, KJ Haworth, SD Swanson, ML Fabiilli, OD Kripgans, PL Carson, JB Fowlkes, University of Michigan, Ann Arbor, MI

Purpose: Acoustic droplet vaporization (ADV) shows promise for the spatial control and acceleration of thermal lesion production. In this study, we investigated the hypothesis that ADV bubbles can substantially enhance HIFU ablation by increasing and controlling local energy absorption. Method and Materials: HIFU/ADV phantoms were made of polyacrylamide, egg white, degassed water and lipid-coated perfluoropentane droplets (1.8 μm mean dia.). These egg white-based phantoms (acoustic attenuation of 0.3 dB/cm at 1.44 MHz) were optically transparent, which allowed direct visualization of lesion formation during HIFU application. Phantoms were exposed in degassed water at 37°C to a focused ultrasound (1.44 MHz) with a focal intensity of 2000 W/cm^2. Lesion volumes were measured by fluid displacement or T2 weighted MR imaging. Results: For 2-s HIFU exposure on droplet-containing